

VISUALIZATION STUDY OF PERFORMANCE BREAKDOWN IN TWO-PHASE PERFORMANCE OF AN ELECTRICAL SUBMERSIBLE PUMP

by

Jose Gamboa

Technology Specialist

and

Mauricio G. Prado

Associate Professor, Petroleum Engineering Department

University of Tulsa

Tulsa, Oklahoma

Jose Gamboa has been Technology Specialist for Multiphase System Integration since 2009, at the University of Tulsa, in Tulsa, Oklahoma. He has eight years of industrial experience, gathered from 1995 to 2003, when working as a production engineer in the areas of artificial lift for Petroleos de Venezuela in Brazil. His main areas of interest include artificial lift, production optimization, and multiphase flow modeling.

Dr. Gamboa holds a B.Sc. degree (Mechanical Engineering) from Universidad Metropolitana, a M.Sc. degree (Mechanical Engineering) from Universidad Simon Bolivar, and his Ph.D. degree from the University of Tulsa. He is a member of the Society of Petroleum Engineers and American Society of Mechanical Engineers.

Mauricio G. Prado is Associate Professor of the Petroleum Engineering Department of the University of Tulsa, in Tulsa, Oklahoma. He is also Director of the University of Tulsa Artificial Lift Projects, an industrial academic cooperative research consortium. He joined the Petroleum Engineering Department in 1999. Dr. Prado has 16 years of industrial experience, gathered from 1983 to 1999, when working as a production engineer in the areas of artificial lift and multiphase flow for Petrobrás in Brazil. His main areas of interest include artificial lift, production optimization, and multiphase flow modeling.

Dr. Prado holds a B.Sc. degree (Metallurgical Engineering) from Instituto Militar de Engenharia, a M.Sc. degree (Petroleum Engineering) from Universidade Estadual de Campinas, and his Ph.D. degree from the University of Tulsa. He is a member of the Society of Petroleum Engineers, American Society of Mechanical Engineers, and Petroleum Society of the Canadian Institute of Mining, Metallurgy, and Petroleum.

ABSTRACT

Barrios (2007) conducted an experimental work in which was demonstrated that the two-phase stage performance of an electrical submersible pump (ESP) is related to the impeller gas and liquid flow pattern as mentioned by Murakami and Minemura (1974a) for a volute-type centrifugal pump. Barrios (2007) proved that the stage head breakdown is a consequence of the gas pocket formation in the impeller channel as in a volute type pump. However, the gas pocket is described as unstable by Murakami and Minemura (1974a) so a slug-flow-like pattern is observed in the impeller channel at the head breakdown condition. Barrios (2007) observed that the gas segregates near the back shroud after the gas pocket formation so that it is stable and a gas segregated pattern is observed into the impeller. The discrepancy between both studies may imply that different mechanisms are acting in the gas pocket formation and its stability, which finally affects the stage performance.

The objective of this research is to study the gas pocket behavior through the visualization of the flow pattern within an ESP impeller at different operating conditions and fluid properties. Therefore, a series of experimental tests has been conducted utilizing a two-stage prototype at rotational speeds between 600 rpm and 1000 rpm, 2 psig inlet pressure and volumetric gas fraction up to 10 percent. This prototype was built with a transparent acrylic casing to observe the flow pattern within the impeller, at the diffuser region and at the impeller inlet region. The gas and liquid flow patterns are observed from videos taken with high speed cameras. Two ports for gas injection have been disposed so the gas can be injected directly to the impeller inlet to get the single stage performance or through the first stage to obtain the multistage performance. A combination of different fluids such as distilled water and air, distilled water and sulfur hexafluoride, and air and a mixture of isopropanol (IPA) and water was utilized in this study.

The videos show that the gas pocket is small and located near the front shroud at liquid flow rates higher than stage best efficiency point (BEP). It is formed and dragged out by liquid flowing over the gas pocket as mentioned by Murakami and Minemura (1974a). The gas pocket becomes stable once it has grown through the channel cross section area when the liquid flow rate is reduced down to BEP. At this operating condition, the gas pocket reduces the upper flowing area and forces the liquid to flow in the remaining area between the gas pocket and the trailing channel face. Further reduction of liquid flow rate below the BEP causes the gas pocket to segregate forcing the liquid to flow underneath as Barrios (2007) mentioned. The gas pocket is formed even at zero head, which demonstrates that it is a consequence of bubble coalescence within impeller channel. The critical gas fraction for the gas pocket formation varies as a function of gas density while its stability and formation is a function of the surface tension and bubble size.

INTRODUCTION

The electrical submersible pump (ESP) is a type of centrifugal pump, which is classified as a multistage vertical pump with a diffuser casing. Due to its high efficiency and compact design, the ESP is widely utilized in a variety of areas, such as: artificial lift, subsea boosting and water injection, among other applications. As an artificial lift system, the ESP literally works "submersed" into the fluid, since it is installed within a cased hole well from which the oil is produced. In most of these cases, the ESP is utilized for high productivity oil wells, high water cut oil wells, dewatering coalbed methane (CBM) wells, heavy oil wells, and it has recently been used as a seafloor boosting method for deepwater subsea wells.

The performance testing, head curve representation, recommended practices for design and installation of ESP systems are prescribed by the American Petroleum Institute (API RP 11S2, 1993). Based on these standards, the stage performance is specified instead of

the overall pump performance. Generally ESP pumps can create head up to 50 feet of water per stage, and have a pump capacity from 100 bpd up (3 gpm) to 90,000 bpd (2,625 gpm).

Because the ESP pumps are centrifugal pumps, liquid viscosity and free gas can affect their performance. Neither the viscosity nor the free gas effects on the stage performance is fully understood at the present time. Nevertheless, the gas effect is a major concern in artificial lift applications, since the gas presence deteriorates the pump lifting capability and causes pump blockage at higher volumetric gas fractions. A large number of studies have been carried out on this topic, focusing on the development of correlations for predicting the two-phase head as a function of the volumetric gas fraction.

By analogy to two-phase flow in pipes, different gas and liquid flow patterns occur inside the impeller channels, which are classified as follows: bubbly flow, elongated bubble, and gas blockage (Duran, 2003). The surging is associated with the formation of a gas pocket in the low pressure side of the impeller channel (Estevam, 2002; Barrios, 2007). The problem is to determine when, how and what causes the gas pocket formation and the surging. The mechanism that triggers the gas pocket formation is expected to be a function of pump type, impeller geometry, rotational speed, liquid flow rate, volumetric gas fraction, fluid properties, and intake pressure.

LITERATURE REVIEW

Two-Phase Pump Performance

Murakami and Minemura (1974a and 1974b) conducted the first comprehensive study on gas effects on the performance of a centrifugal pump. Based on extensive experimental tests conducted with air and water, they demonstrated that the pump head is altered by gas presence. Murakami and Minemura (1974a) observed that the deterioration of the pump head is a consequence of the gas-liquid flow pattern within the impeller. Thus, the change in deterioration rate is due to the transitions between the flow patterns.

In a later work, Murakami and Minemura (1974b) studied the effect of impeller geometry on the two-phase pump performance. The authors carried out a new set of experiments with three pumps that had the same impeller diameter and the same impeller type but had different number of blades (3, 5, and 7 blades). They found that the two-phase performance of the pump with the smaller numbers of blades was different from that of the other two pumps. For this pump, the pump head at low gas volumetric fraction (point 1 in Figure 1) slightly improved as compared to the single-phase performance (point 0 in Figure 1).

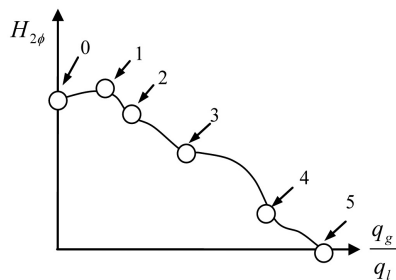


Figure 1. Two-Phase Head Variation with Gas-Liquid Ratio. (Courtesy Murakami and Minemura, 1974b)

Murakami and Minemura (1974b) explained that such performance is caused by the air bubbles, which “intensify the unevenness of flow velocity and shift the main flow more to the suction side of the impeller.” Hence, the peripheral component of the absolute velocity changes, causing an increment in the pump head. Any further increase of gas liquid ratio resulted in a deterioration of the pump head as explained before. These experimental results demonstrate the effect of pump geometry in two-phase pump performance. The previous description of the two-phase performance

of centrifugal pumps is widely accepted and experimentally verified by Manzano-Ruiz (1980) and Sato, et al. (1996), among other authors.

The two-phase performance presented so far corresponds to the volute-type single-stage centrifugal pump. The first study on the two-phase performance of ESPs or vertical pumps with diffuser casings was conducted by Lea and Bearden (1980). The authors performed a series of tests at low and high pressure, utilizing one type of radial impeller pump and two different mixed type impellers. The low pressure tests were performed with air and water while carbon dioxide and diesel were utilized in the experiments at high pressure.

The authors classified the two-phase stage performance into four categories: nongas interference, gas interference, intermittent gas lock and gas lock. When the volumetric gas fraction is low, the two-phase stage performance is the nongas interference regime and the performance remains the same as that of the single-phase performance. At higher volumetric gas fractions, the gas interference begins to be noticed causing a deviation from the single-phase head curve. Higher volumetric gas fractions lead to an intermittent gas locking regime where the stage head shows low frequency oscillations, which are also observed in the pump flow rate. Further increase of gas fraction from this regime causes the pump head to breakdown, which was termed the gas lock regime.

Experimental results demonstrated that the gas causes the same deterioration effect in the stage head of a multistage pump as that observed in single-stage volute-type pumps. Furthermore, the two-phase stage performance is altered by the rotational speed, inlet pressure, free gas at inlet conditions and impeller type. The effect of impeller type is one of the most important conclusions from this study. The experimental results showed that mixed type pumps exhibit a better two-phase performance than the radial type pumps.

Since Lea and Bearden’s (1980) experiments were conducted with multistage pumps, the stage performance reported was an average from the overall pump performance. This meant that the pump head was determined from the discharge and intake pressures divided by the number of stages and the average mixture density, in order to obtain the head in feet of water. The average mixture density is calculated from the gas and liquid densities and volumetric gas fraction at discharge and inlet operating conditions. This procedure assumes that the stage performance is the same as is expected in a serial pump arrangement. However, Pessoa (2001) demonstrated that this averaged stage performance differed from the actual two-phase performance of the stages in an ESP and therefore all studies on the two-phase performance should be made on a stagewise basis.

Pessoa (2001) mapped stage by stage performance of a 22-stage ESP handling air and water at a constant intake pressure and rotational speed. His results show that the performance of every stage varies along the pump. Pessoa (2001) also observed that the contribution to the overall head of the first stages differ significantly from the other stages. In some conditions, the first stages were actually dissipating pressure while the remaining stages were responsible for developing a useful pressure. The downstream stages usually presented a better performance.

Further study on the two-phase stage performance was conducted by Duran (2003). He found that large uncertainties could carry on by measuring the stage pump head through absolute pressure sensor. Therefore, he installed a differential pressure transducer only in the 10th stage of a 22-stage ESP pump so that the pressure rise of this stage could be measured with more accuracy. His experiments were performed at a constant rotational speed, constant mass gas rate and intake pressure, while the liquid flow rate was reduced from the fully open choke flow rate to the shut-off head. Duran (2003) observed slope discontinuities in stage head similar to those mentioned by Murakami and Minemura (1974a). Nevertheless, he classified the stage performance in three regimes: bubbly flow, transition, and elongated bubble flow, following the classification proposed by Estevam (2002).

In the bubbly flow regime, the pump head deteriorates due to the gas presence. This deterioration can be mild or severe, depending on the mass gas rate handled by the pump. In Duran's (2003) experimental data, the pump head breakdown marked the transition between the bubbly flow regime and the transition regime. In the transition regime, the head slope with respect to the liquid flow rate reverses its sign so the pump head drops as the liquid flow rate is reduced. As a result, instabilities of the liquid flow rate, pump head, and inlet pressure are observed. This trend terminates in the elongated bubble regime, where the pump head becomes almost flat and independent of the liquid flow rate. The experimental data demonstrated that the pump head breakdown is affected by the stage inlet pressure, the liquid flow rate, and the gas mass flow rate.

Zapata (2003) conducted tests similar to Duran's (2003), but Zapata (2003) studied the effect of the rotational speed on the two-phase stage performance. He observed the same three discontinuities detected by Duran (2003) and described the performance utilizing the same regime classification. However, Zapata (2003) noticed that the bubbly flow regime was extended toward higher volumetric gas fractions as the rotational speed increased. The other regimes were not altered by the variation of the rotational speed.

Impeller Flow Patterns

Murakami and Minemura (1974a) utilized high speed film and high speed photography to observe the impeller flow pattern and bubble behavior at different operational conditions. Based on their visual evidence, Murakami and Minemura (1974a) identified four flow patterns within the pump impeller: isolated bubble flow, bubbly flow, slug flow, and segregated gas.

The first impeller flow pattern was observed at very low volumetric gas fractions. Murakami and Minemura (1974a) mentioned the bubbles at this operating condition are so distant from each other that interaction between them is negligible. These bubbles flowed undisturbed through the impeller channel alone or "isolated." As a consequence, the liquid streams remained unaltered and the pump head was the same as that of single-phase. A second flow pattern is observed at slightly higher volumetric gas fraction where a very organized bubbly flow pattern is then observed. The bubbles into the impeller still follow the liquid stream lines, although, there is more interaction between them respect to the previous condition. At this flow pattern, the pump head is not longer equal to the single-phase.

Further increase of the volumetric gas fraction leads to another flow pattern transition. Murakami and Minemura (1974a) suggested the elevated number of bubbles cause an increment in the number of collisions between bubbles. It promotes the bubbles to coalesce and form a void or air pocket at the impeller inlet region. The authors observed this air pocket is constantly dragged out and reformed, resembling slug flow in pipes. Murakami and Minemura (1974a) classified this transition as bubbly flow-slug flow transition. The pump head breakdown previously mentioned coincides with this flow pattern transition.

Pump operation in the slug flow regime is unstable and low frequency oscillations were observed in the pump head and rates. The pump resumed its steady operation once the air pocket reached a certain "equilibrium" point at a higher volumetric gas fraction. This operating condition marked the transition from slug flow to a segregated flow. Murakami and Minemura (1974a) characterized the segregated flow regime by a large air pocket being stuck at the inlet impeller region, forcing the water to flow underneath it. At even higher volumetric gas fractions, the air pocket took over the entire channel area and the pump and the head became almost zero.

Murakami and Minemura (1974b) pointed out that the number of blades can affect the bubble behavior in the isolated bubble flow pattern. However, no noticeable effect can be seen in the other flow patterns. Nevertheless, the rates where the transitions occurred can be modified by the number of blades. For instance, the transition

between bubbly flow and slug flow happens at lower volumetric gas fractions in impellers with a smaller number of blades (Murakami and Minemura, 1974b). On the other hand, Downham (2000) found that the air pocket is formed only in divergent impeller channels while a steady bubbly flow is always observed in parallel straight impeller channels.

Estevam (2002) and Barrios (2007) conducted a series of visualization tests with ESPs. Based on observations from both studies, it can be concluded that Murakami and Minemura's (1974a) flow pattern classification and description are also applicable to ESPs.

ESP PROTOTYPE AND SINGLE-PHASE PERFORMANCE

Background

An ESP stage consists of two diffusers that form a housing, into which the impeller rotates, as is presented in Figure 2. The diffuser located at the impeller entrance is known as "intake diffuser" and its function is to straighten the fluid coming into the impeller, in order to minimize fluid prerotation. The top diffuser termed "discharge diffuser" leads the fluid away from the impeller and transforms the high fluid velocity at impeller exit into pressure. Both diffusers are geometrically identical in every stage except in the first and last stages, where modified ones are utilized.

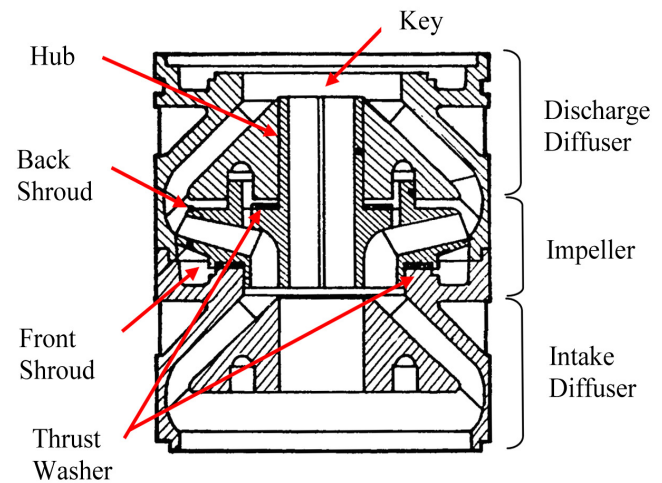


Figure 2. Schematic of ESP Stage.

The impellers utilized in an ESP are a closed-type, either radial or mixed flow type. The driving shaft is installed into the impeller hub with a transitional fit tolerance that permits its axial movement. A key shaft placed between the driving shaft and the impeller attaches them together. Any possible impeller misalignment is corrected at the intake diffuser, which works as a guide for the impeller. This configuration is called "floating impeller stage."

Both the impeller and diffuser are made from high carbon content steel usually through a metal casting manufacturing process. Accordingly, the assembling requires precise tolerances in order to avoid a metal to metal contact. Therefore, composite thrust washers are placed at the front and back shrouds, in order to avoid premature failure.

New Visualization Stage

Based on this description, one can understand that visualization of the fluid inside of an ESP stage is an impossible task, unless the stage geometry is somewhat modified. Barrios (2007) overcame this problem by building a two-stage prototype based on the geometry of a commercial ESP. This solution is also adopted in this study.

Therefore, a new visualization stage was built for Barrios (2007) prototype, which is shown schematically in Figure 3. As can be

seen, the casing is a combination of commercial transparent acrylic tubes, with a flange at the lower edge. The discharge diffuser is accommodated within a 5 inch diameter transparent acrylic tube, inside which another tube of 4.5 inch diameter is inserted. This configuration creates a small lip over which the diffuser is seated. The 4.5 inch tube is extended 1.73 inches to create a housing for the impeller. An acrylic ring is inserted into this tube, which reduces its diameter to 2.75 inches. Next, a 3.25 inch diameter tube is glued to this ring and extended 2.18 inches, to a 6 inch flange made from the same material. This flange is utilized to fix the prototype to the lower stage of Barrios (2007) prototype. A cork seal is placed between the acrylic flange and the metallic casing of the first stage, in order to avoid leaks.

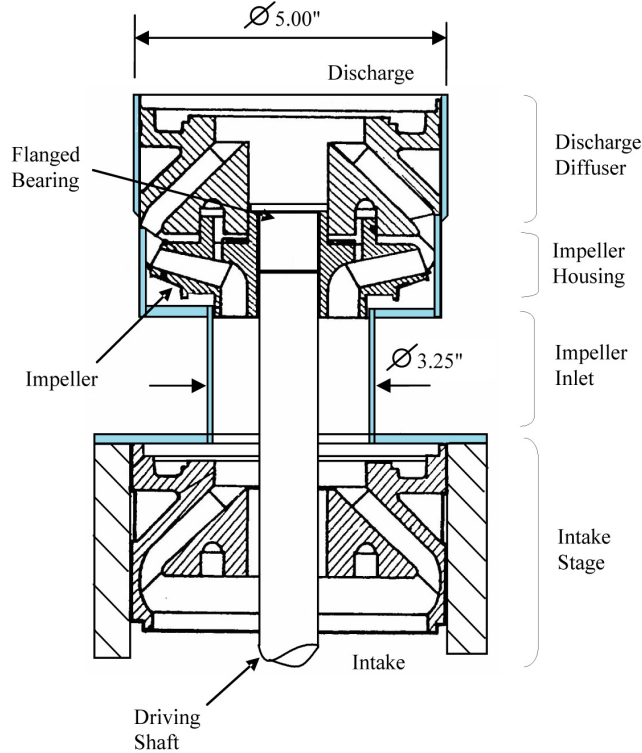


Figure 3. Schematic of New Visualization Stage.

Another 4.5 inch diameter acrylic tube is inserted through the top of a 5 inch diameter tube in order to prevent axial movement of the discharge diffuser. A waterproof silicone is applied in the border line between the steel diffuser and the acrylic tube, aiming to prevent diffuser rotation.

The diffuser and impeller utilized are from a commercial ESP. However, the diffuser outer wall has been removed, so that the diffuser vanes at that region are exposed. The purpose of this modification is to create a “window” around the impeller for visualization purposes. The prototype impeller is “floating,” as is in an actual ESP. However, the downthrust movement is limited by a flanged bearing fitted with a tight tolerance into the shaft hub. This prevents contact between the impeller and the acrylic housing.

The manufacturer catalog and the prototype performance curves for water are compared in Figure 4. The original pump is a 5.00 inch ESP with a specific speed, N_s , estimated to be 3,300. The prototype performance matches the manufacturer performance curve at flow rates near the best efficiency point, which is depicted as a dot line in this figure. The prototype curve falls below the manufacturer curve for any other liquid flow rate, away from the BEP. In fact, the shutoff pressure rise is reduced 18 percent while the flow rate at fully open choke is 17.5 percent smaller with respect to the manufacturer’s curve.

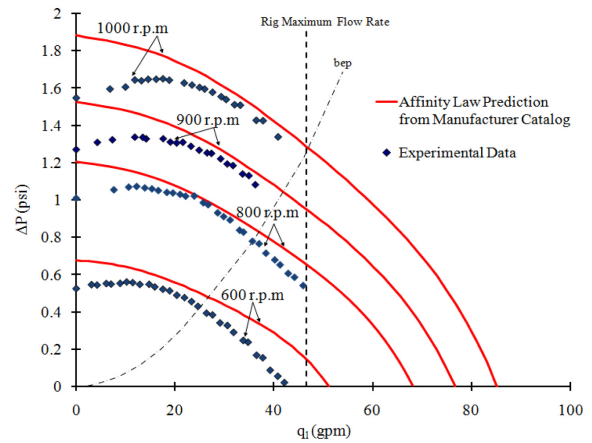


Figure 4. Comparison Between Manufacturer and Prototype Performance Curves.

In order to find the reason of such discrepancy, a new test has been conducted seeding the water with 1 mm Styrofoam beads. Figure 5 shows photos of a foam bead passing through the gap between the diffuser vane and the acrylic casing. It demonstrates that the lack in performance is a consequence of the liquid flow through this gap. The prototype performance is then severely affected by the leak or recirculation through diffuser vanes at liquid flow rates away from the BEP. This problem could not be solved because the integrity of the prototype could be compromised. Accordingly, the tests go on despite this performance problem.

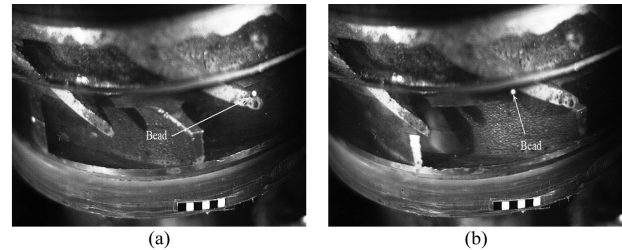


Figure 5. Foam Bead Trajectory.

EXPERIMENTAL PROGRAM

Experimental Facility

A layout of the facility is presented in Figure 6. This rig consists of a 15 gallon cylindrical plastic tank that serves as a water storage tank and separator. This tank supplies water utilizing a 1.5 hp single stage centrifugal pump, which works as a booster pump. The tank and the booster pump are connected through a 2 inch PVC pipe, in which a 2 inch brass gate valve (V-3) has been installed, to isolate the tank for maintenance and cleaning. The booster pump is connected to the prototype stage through another 2 inch PVC pipe that accommodates a 1.5 inch turbine flow meter (F-1), for metering the liquid flow rate.

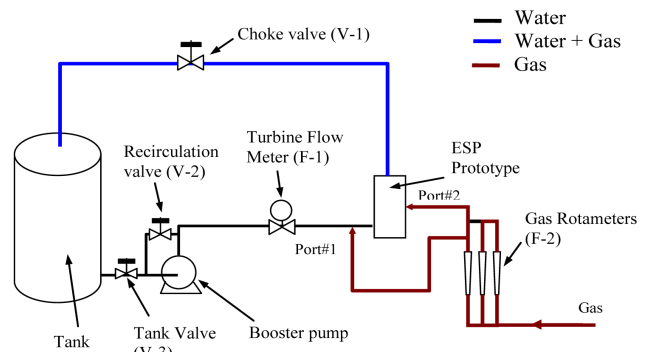


Figure 6. Experimental Facility Layout.

The fluids leaving the prototype return to the tank through another 2 inch PVC pipe equipped with a 2 inch brass gate valve (V-1). This valve is utilized for choking the prototype during the single-phase tests, and controlling the intake pressure during the two-phase experiments. The connection between the prototype and the loop pipelines is made through two flexible polypropylene reducing couplings.

Two ports (#1 and #2) are installed for gas injection and one port (#3) for Styrofoam beads injection (Figure 7). The first port is located at the inlet pipe, whereby the gas injected flows through the prototype first stage, prior to the visualization stage. The second port is located 4 inches from the impeller of the visualization stage. Therefore, gas can be directly injected into the impeller. The last port is a 1/8 inch hole made in the stainless steel casing of the first stage. This allows access to the discharge diffuser of the first stage.

The air is supplied from a 1 hp air compressor delivering pressure up to 10 psig and flow rates up to 10 standard cubic feet per hour (scfh). Other gases are supplied from a high pressure vessel equipped with a double stage choke regulator. A series of rotameters (F-2) is installed for gas flow rate measurement. Each rotameter is equipped with an internal needle valve that is utilized to regulate the gas flow rate during the experiments. The values read from the rotameters are corrected based on gas molecular weight.

The liquid flow rate is regulated by either varying the booster pump rotational speed or adjusting the 1 inch gate valve (V-2), which is utilized to recirculate the liquid at the booster pump. The prototype is driven by a 5 hp squirrel cage motor, whose rotational speed is regulated from a variable speed driver. A handheld tachometer is utilized for measuring the rotational speed.

Two differential pressure transmitters have also been installed, as is shown in Figure 7. The differential pressure (DP-1) measures the stage pressure rise, while the other differential pressure (DP-2) is utilized to acquire the total pressure rise generated by the two stages. The absolute pressure transmitter (PT-1) measures the intake pressure. The water temperature is measured in the tank through a type-T portable thermocouple.

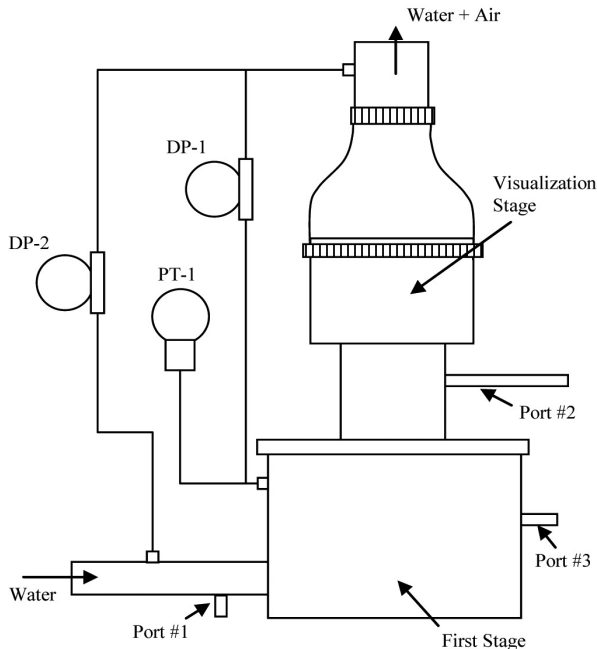


Figure 7. Injection Ports Location.

Flow Visualization

A high speed CCD camera model (camera 1) is utilized to record the fluid flow inside the impeller. This camera is able to record videos at 1,000 frames per second (fps), with an image resolution of 800 × 600 pixels. The camera can be set at a higher frame rate,

but it causes a dramatic reduction of the image resolution, as stated by Barrios (2007). The camera is capable of recording up to 4 seconds of continuous video in AVI uncompressed format. This format offers a great image resolution, but the size of every video is of the order of gigabytes. This requires up to two hours in order to record and save 4 seconds of video. Therefore, the recording time in every video is limited to 1 second, which takes an average of 25 minutes to be saved into the camera memory.

For the current experiments, the frame rate is set at 600 fps and the shutter speed is varied between 40 μs and 100 μs. The sharpness of the image is the criterion utilized to set both parameters, which was accomplished after several adjustments in preliminary trials.

Because the frame rate is constant, the number of pictures per revolution varies with the rotational speed. As a consequence, the rotational speed in the experiments is limited at 1,000 rpm, which allow that only five pictures of an impeller channel are taken per revolution.

Another parameter to be set is the depth of focus. It is “the range of distance along the optical axis in which the specimen can move without the image appearing to lose sharpness” (Ray, 1997). The depth of focus depends on the lens exposure and the distance between the camera and the target, which is called “magnification.” Although the distance between the camera and the prototype is kept constant, the lens exposure is varied in order to increase the image sharpness in a certain spot inside the impeller. This implies that the depth of focus is set at a certain region of the impeller channel.

Another high speed camera (camera 2) was used to acquire the videos of the fluid at the impeller inlet region. This camera can record a high speed video at 300 fps with a resolution of 512 × 384 pixels. The shutter speed is set to 400μs, while the lens exposure and depth of focus are adjusted to increase the sharpness of the image.

In terms of lighting, three 120 Watts ultra high performance (UHP) mercury arc lamps are utilized. These lights are capable of producing a high intense light beam whose luminance exceeds 9,000 lumens. The color temperature of these lamps is around 10,000 K.

Camera 1 is fixed at 45 degrees at a distance of 10 inches from the visualization stage. This camera is held in place with arms, which are fixed in a prototype based by a super clamp. The same type arms are also utilized to fix the light sources, which are installed diametrically opposed to each other, forming an arc of 30 degrees around camera 1. The other source is located at the bottom of the impeller at a certain angle, which can be varied to regulate the background illumination. Camera 2 is manually held at 5 inches from the transparent casing.

Test Fluids

Distilled water and air are utilized to establish the experiment baseline for a noncondensable system, whereby its properties are given in Table 1. Next, sulfur hexafluoride (SF₆) is utilized instead of air in order to study the effect of gas density in the two-phase stage performance. This gas is an odorless and harmless gas that is approximately six times heavier than air at atmospheric conditions. The surface tension between the water and SF₆ is fairly close to the air and water surface tension and it has a very low solubility in water, as is shown in Table 1. The SF₆ becomes liquid at pressure above 320 psig at 78°F so that the experiments made with this gas are for a noncondensable system.

Table 1. Fluid Properties.

	Water	Air	SF ₆
Specific Gravity	1 @ 60° F	1 @ 60° F, 1 atm	5.11 @ 60° F, 1 atm
Viscosity (cP)	1.12 @ 60° F	0.0179 cP @ 60° F, 1 atm	0.015 cP @ 77° F, 1 atm
Surface Tension (dyne/cm)	-	72.8	71.6 @ 60° F
Molecular Weight	18.15	29.8	146.05
Solubility in Water	-	0.023 g/L @ 68° F, 1 atm	0.04561 g/L @ 68° F, 1 atm

The density of the gases is determined from real gas law based on the temperature and pressure of the experiments. In the case of SF₆, the deviation factor is calculated by the Redlich-Kwong (1949) equation of state.

The effect of surface tension on the two-phase performance of an ESP stage is investigated utilizing a mixture of water and the isopropyl alcohol or isopropanol. Table 2 shows the surface tension for the two IPA concentration tested. The same set of tests that have previously been mentioned is repeated for these two IPA concentrations.

Table 2. Water/Alcohol Surface Tension.

Alcohol Concentration (%)	Surface Tension (dynes/cm)
0.505	67.40
1.234	62.52

Experimental Procedure

The procedure adopted to carry out the visualization experiments was established after several preliminary tests. Thus, the tests are performed by keeping the liquid flow rate constant and varying the gas flow rate. In every test, the liquid flow rate, gas flow rate, intake pressure, and rotational speed are fixed to their setting values. Once the flow condition reaches steady-state, a file with the pressure and liquid flow rate data is saved for at least 1 minute (350 points). Next, the videos are recorded.

First, a video of the flow inside the impeller is acquired with camera 1 and then a second video is recorded with camera 2 in the impeller inlet region. If the gas is injected directly to second stage, Styrofoam beads are injected through port #3 at the same time with the gas and the water. Thus, an extra video is recorded with the gas, liquid, and beads flowing simultaneously through the impeller.

Next, the gas flow rate is adjusted to a new setting value and the system is regulated to keep the liquid flow rate and intake pressure constant. Once this condition is stable, the system is shut down until camera 2 finishes saving the video. Then, the system is turned on and the procedure is repeated.

Experimental Test Matrix

The experimental test matrix is based on the normalized gas and liquid flow rates. The normalized gas flow rate, q_{gd} , is defined as:

$$q_{gd} = \frac{q_g}{q_{max}} \quad (1)$$

where q_g is actual gas flow rate at stage intake pressure and temperature while q_{max} is the single-phase flow rate at fully open choke at certain rotational speed. The normalized liquid flow rate q_{ld} is given as ratio of actual liquid flow rate (q_l) and q_{max} , as shown in Equation (2).

$$q_{ld} = \frac{q_l}{q_{max}} \quad (2)$$

Three sets of experiments have been conducted, as summarized in Table 3. The first set was carried out with water and air for normalized liquid rate between 0.2 and 0.6 at 600 rpm, injecting the air directly to the second stage (port #2). The additional experiments were performed at 800 rpm and 1,000 rpm, utilizing the same injection port for 0.6 normalized liquid rate. Next, the same tests were repeated, but injecting the air through the first stage (port #1).

Table 3. Experimental Test Matrix.

Fluids	Gas Injection Point	Normalized Liquid flow rate (q_{ld})	Pump speed (rpm)
Air and Water	Impeller Inlet and Pump Inlet	0.6	600
			800
			1,000
		0.8, 0.4, and 0.2	600
SF6 and Water	Impeller Inlet and Pump Inlet	0.6	600
Air and Alcohol Aqueous Solution	Impeller Inlet and Pump Inlet	0.6	600

The second set of experiments was performed with SF₆ and water. In this case, the tests were performed only at 600 rpm for a normalized liquid rate of 0.6. First the gas is injected through port #2 and then the same test is conducted injecting the gas through port #1. Finally, the last experimental set was carried out with air and IPA aqueous mixture. Once again, tests were carried out only at 600 rpm for 0.6 normalized liquid rate varying the gas injection port.

The maximum rotational speed for the experiments is set at 1,000 rpm due to the limitation of the video resolution. Most of the experiments are carried out at 600 rpm since this is the maximum rotational speed in which the stage performance can be observed from zero pressure rise until the shut-off condition.

In every test the stage pressure rise (Δp) is measured utilizing differential pressure (DP-1). The volumetric gas fraction (λ) is calculated as:

$$\lambda = \frac{q_g}{q_g + q_l} \quad (3)$$

where the liquid flow rate (q_l) is measured by the turbine flow meter (F-1) while gas flow rate is measured by gas rotameter (F-2) and later corrected at the second stage intake pressure (PT-1) and liquid temperature measured at the tank.

EXPERIMENTAL RESULTS

Air-Water Performance Curves

The performance curves for air and water flow are shown in Figure 8 at normalized liquid rates between 0.2 and 0.8 and 2 psig stage intake pressure (stage #1), where the air is injected through the first stage. In this figure, the stage pressure rise (Δp) is presented as a function of the volumetric gas fraction (λ), for a constant normalized liquid rate. Notice that the stage pressure rise mildly deteriorates as the volumetric gas fraction increases, until a sudden performance breakdown occurs. Such a behavior matches the performance description mentioned in the previous chapter.

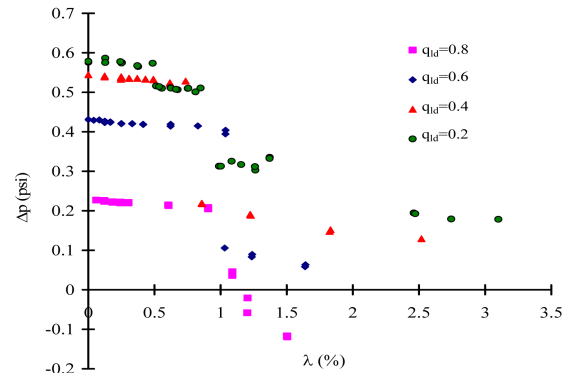


Figure 8. Air/Water Flow Performance Curves. From 0.2 to 0.8 Air is Injected Through the First Stage.

The surging, which is identified as the performance breakdown occurs at volumetric gas fractions of 0.48 percent, 0.73 percent, and 1.03 percent for a normalized liquid rate of 0.2, 0.4 and 0.6, respectively. These results show that the surging moves to lower volumetric gas fractions for liquid flow rates smaller than the best efficiency point.

The change of slope observed in the performance curve at 0.9 percent volumetric gas fraction for 0.8 normalized liquid rate is the surging occurring at high liquid flow rate. It is confirmed by the videos that a gas pocket is formed within the impeller at this operating condition, as is explained in the next section. Contrary to the jump observed at other liquid flow rates, the surging for this normalized liquid rate is identified as a variation of the performance curve slope, which becomes a function of the volumetric gas fraction. Thus, it is constant before the surging and then becomes a function of the gas rate after it.

Gas Injection Effect

Figure 9 shows the stage pressure rise data obtained for air/water at 600 rpm and 2 psig stage intake pressure (stage #2) for volumetric gas fractions up to 1.3 percent, whereby the air is injected directly to the second stage (port #2).

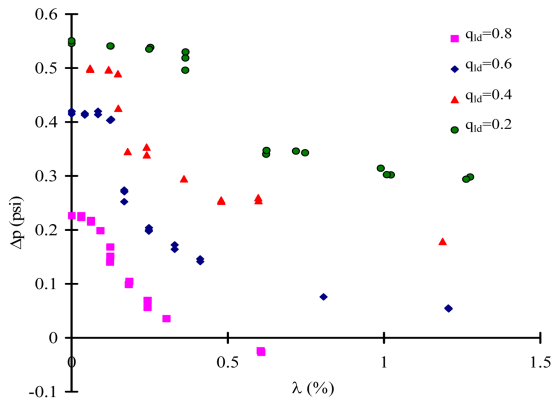


Figure 9. Air/Water Flow Performance Curves. From 0.2 to 0.8 Air is Injected Through Directly to the Second Stage.

The departure from the single-phase performance can be clearly observed in performance curves for normalized liquid flow rates between 0.2 and 0.6. This deterioration in performance is not severe until the surging, which occurs at volumetric gas fractions of 0.12 percent, 0.14 percent and 0.36 percent for normalized liquid rate 0.6, 0.4 and 0.2, respectively. After the surging, the pressure rise continues reducing with the increase of the volumetric gas fraction.

These results demonstrate that the surging tends to move to a higher volumetric gas fraction as the liquid flow rate is reduced, which differs from the performance observed when the gas is injected through port #1 at the same stage intake pressure.

The performance curve at 0.8 normalized liquid flow rate differs from the previous description. The deterioration rate for this normalized liquid flow rate is higher than the other ones. The stage loses 44 percent of its pressure rise when the surging happens at 0.12 percent volumetric gas fraction. A small decay in the pressure rise is observed in the surging so that the pressure rise falls 0.03 psig, after which it continues decreasing until it becomes negative at a volumetric gas fraction of 0.51 percent. According to the high speed videos, the small pressure rise decay in the surging is caused by the formation of a gas pocket, which is unstable as explained in the next section.

Because the pressure at the visualization stage intake is kept constant during the experiment, it is hard to conclude that the decrement of gas handling by the stage is due to density variation. An important hint comes from the bubble size measurements made at that location. Bubbles up to 3.5 mm are observed at the impeller

inlet region when the gas is injected through port #2, while bubbles with sizes smaller than 500 micron are seen at the same location when port #1 is utilized. The enhanced gas handling capability is strongly tied to the bubble size at the inlet region based on the experimental results. It contradicts Murakami and Minemura (1974b) who concluded that bubble size does not affect the performance of centrifugal pumps.

The smaller bubble observed after the fluids have flowed through the first stage confirms that a bubble breakup phenomenon takes place within the stage. Thus, the first stage works as a “flow conditioner” or “bubble breaker” for the second stage in the serial arrangement utilized.

Rotational Speed Effect

Figure 10 and Figure 11 present the two-phase stage performance at 600 rpm, 800 rpm, and 1,000 rpm for a 0.6 normalized liquid flow rate at 2 psig, varying the air injection port. As observed, the surging moves to higher volumetric gas fraction, as the rotational speed increases, independently of the air injection port utilized.

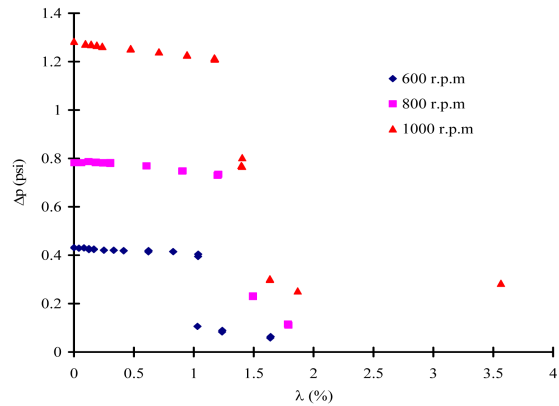


Figure 10. Effect of Rotational Speed, Air Injection Through First Stage.

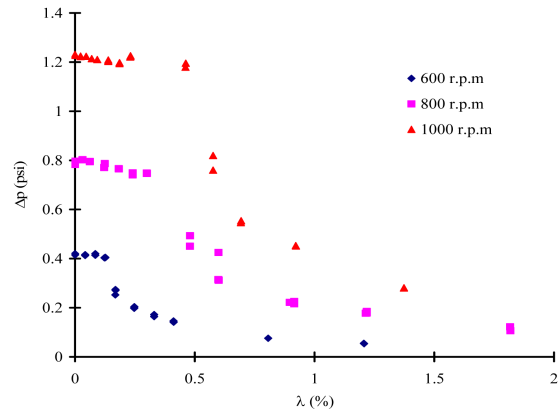


Figure 11. Effect of Rotational Speed, Air Injection Directly to Second Stage.

In Figure 10, one can observe how the surging moves from a volumetric gas fraction of 0.12 percent at 600 rpm to 0.4 percent at 1,000 rpm. It represents an increase of a 2.3 times in the volumetric gas fraction associated with the surging. The equivalent increase is only 25 percent when the gas is injected through first stage.

Gas Density Effect

The effect of gas density on two-phase stage performance has been studied utilizing sulfur hexafluoride. The results of these tests are presented in Figure 12. In this figure, the stage pressure rise with air and water is compared to the stage performance with SF₆ and water, when the gas is injected directly to second stage. Notice

that the stage pressure rise is the same for both cases for volumetric gas fractions smaller than 0.09 percent. The surging occurs at 0.12 percent volumetric gas fraction for the air and water case, while the stage pressure rise with SF₆ remains close to the single-phase head. The surging is observed in SF₆ performance curve at a volumetric gas fraction of 0.71 percent. At this volumetric gas fraction, the pressure rise with air is only 0.07 psig as compared to 0.41 psig for the SF₆ case.

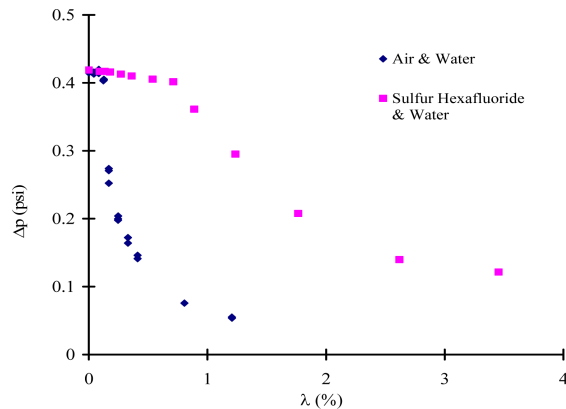


Figure 12. Effect of Gas Density at 2 psig, 600 rpm, =0.6, Gas Injection Through Second Stage.

The effect of gas density on the stage performance is more pronounced when the gas is injected through first stage. Figure 13 shows the performance curves obtained with both gases utilizing water as liquid phase at 600 rpm for 0.6 normalized liquid flow rate and 2 psig stage pressure. To the contrary of the performance previously observed, both curves never overlap even at low volumetric gas fractions. The stage performance with SF₆ remains equal to the single-phase performance for volumetric gas fractions as high as 4.4 percent, where a slight departure from the single-phase performance is observed. The surging happens at 6.83 percent volumetric gas fraction with SF₆, in contrast to 1.04 percent with air. The pressure rise in which the surging occurs is approximately the same, which suggests that surging may be related to a certain local critical gas fraction within the impeller, as is mentioned by Minemura and Uchiyama (1983). This critical gas fraction may vary with the liquid flow rate, rotational speed, intake pressure and gas density. These results clearly reveal the dependency of the stage performance to the gas density and indirectly to the intake pressure.

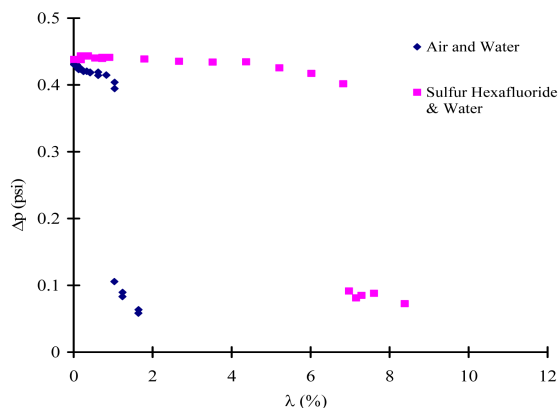


Figure 13. Effect of Gas Density at 2 psig, 600 rpm, =0.6, Gas Injection Through First Stage.

Effect of Surface Tension

The effect of IPA in water when the air is injected through second stage is presented in Figure 14. As can be seen, the curves do not start from the same single-phase pressure rise due to a slight

variation in the liquid flow rate during the tests. Nevertheless, one can observe that the surging moves to higher volumetric gas fractions when IPA is added. Indeed, the volumetric gas fraction at the surging almost double because of the IPA addition.

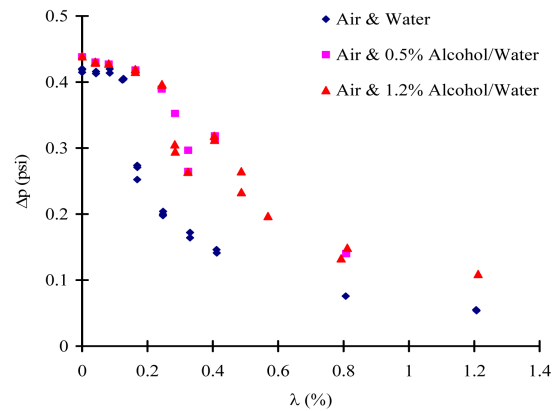


Figure 14. Effect of IPA Concentration at 2 psig, 600 rpm, =0.6, Air Injection Through Second Stage.

The variation of the surging may be associated to the reduction of the water surface tension as is shown in Table 2. A surface tension reduction can cause a reduction in the particle size that may affect the stage performance. This hypothesis was assessed through additional tests at a higher IPA concentration. As can be observed in Figure 14, the increase in the IPA concentration does not change the stage performance. Thus, the reduction of surface tension alone does not cause the performance variation as compared to the pure water case.

Hu, et al. (2006), mentioned that low concentrations of IPA cause a change in the polarization of the bubble surface. The authors suggested that consequence of this change in polarization “the hydrophilic part directed into the aqueous phases and the hydrophobic part into the gas phase, causing the bubble coalescence is heavily suppressed.” This implies that the addition of IPA creates a “noncoalescing” system within the stage impeller. Thus, the bubble coalescence that triggers surging in pure water cannot occur at the same volumetric gas fraction with IPA and water mixture because of the increase of interfacial repulsion forces caused by IPA. Thus, the surging is “suppressed” until higher volumetric gas fractions are reached.

This result opens a new research area that is unexplored. The IPA is a surfactant so its effect on the two-phase stage performance demonstrates the role of interfacial forces, which is not only related to the surface tension as is often mentioned in two-phase pump literature. It is actually related to the interfacial polarity and repulsion forces that can suppress that surging. In practical application it means that surfactants (i.e., methyl-ethyl-glycol, MEG) can be injected at the ESP intake to suppress or displace the surging at higher volumetric gas fractions. However, further study is needed in order to find out the type of surfactant and the concentration needed to cause such effect.

A pressure recovery is observed at a volumetric gas fraction of 0.41 percent, which diminishes at higher volumetric gas fractions. This marginal pressure recovery is mentioned by Murakami and Minemura (1974a). However, it is not seen in either of the other performance curves. It is not clear what produces this recovery and why it occurs. Nevertheless, it may be related to the stability of the gas pocket, as will be discussed in the next section.

The stage performance when the air is injected through the first stage is shown in Figure 15. Again, the discrepancy in the stage pressure rise at zero volumetric gas fraction is due to a small difference in the liquid flow rate between both experiments. In this figure, one observes that the stage performance with alcohol aqueous solution is approximately the same with that of the water performance, until the occurrence of the surging.

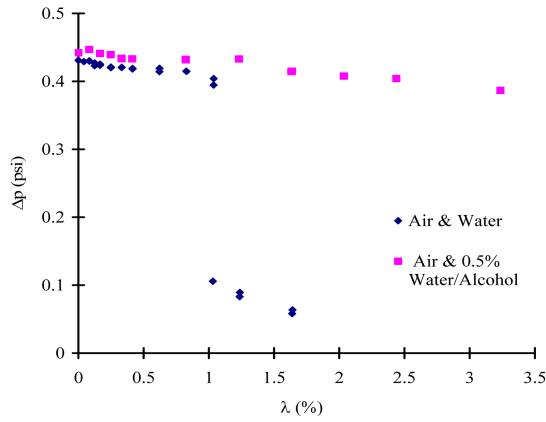


Figure 15. Effect of IPA Concentration at 2 psig, 600 rpm, $\phi=0.6$, Air Injection Through First Stage.

After the surging, the pressure rise drops in the pure water curve. This is in contrast to the pressure rise with alcohol aqueous solution, which remains close to the single-phase pressure rise. The performance curve for IPA and water mixture stays close to the single-phase performance at volumetric gas fractions as high as 3.24 percent. Indeed, the surging could not be observed with this alcohol aqueous solution during the tests at the maximum gas flow rate available.

Impeller Channel Flow Patterns

The impeller channel flow patterns are described based on the performance curve shown in Figure 16. This figure represents the performance curve at 600 rpm, 2 psig, 0.6 normalized liquid flow rate with air injection through the first stage.

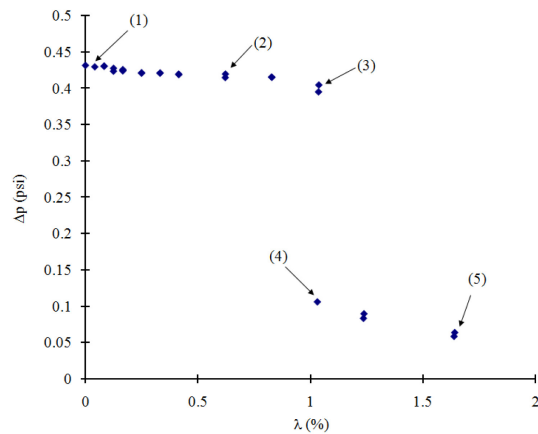


Figure 16. Impeller Flow Patterns (600 rpm, $\phi=0.6$, 2 psig).

Additionally, the flow pattern at the inlet location of the visualization stage is described so the relationship between the impeller channel and the inlet region flow patterns can be qualitatively assessed.

Isolated Bubbles (Regime I, Point (1), Figure 16)

Point (1) corresponds to a volumetric gas fraction of 0.04 percent, in which the stage pressure rise is the same as the single-phase pressure rise. A photo of the flow pattern inside the impeller at this operating condition taken from outer periphery is shown in Figure 17. As observed, “isolated bubbles” are seen flowing within the impeller channel.

The term isolated means that the distance between bubbles is such that there is no interaction between them. A broad range of bubble sizes can be seen, but most bubbles have an equivalent volume spherical diameter smaller than 0.45 mm (450 micron). The

smaller bubbles have a spherical shape, while the intermediate size bubbles have a prolate ellipsoidal shape. The largest bubbles exhibit an irregular shape that can be described as irregular ellipsoidal or egg shape. Most bubbles flow in the region between half of the channel height and the back shroud. However, there are some bubbles that flow close to the front shroud, which often are the largest ones.

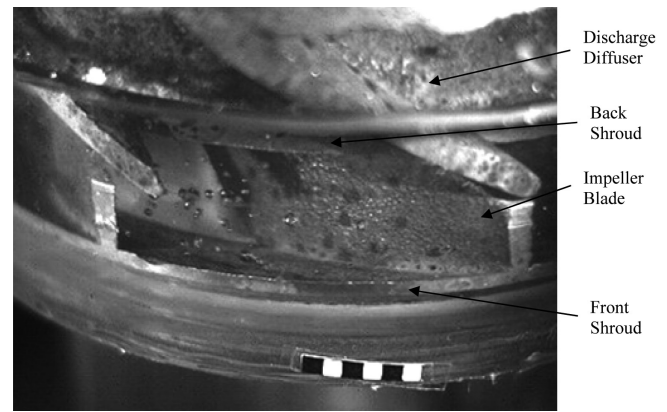


Figure 17. Isolated Bubbles (Regime I, Point (1), Figure 16).

The orientation of the bubbles is constantly changing, which is more noticeable in the prolate bubbles. The orientation of those ellipsoidal bubbles is “random” with respect to the liquid stream. Nevertheless, the major diameter of these bubbles is always parallel to the front shroud. The orientation of these bubbles undergoes a drastic change in the impeller exit region, where they spin and align their major diameter normal to the front shroud. Next, they quickly move up leaving the impeller. The change of orientation happens in the region where there is no back shroud, which indicates that gravity and liquid stream play important roles in the bubble motion, despite the intense centrifugal field in this region.

Figure 18 shows a photo of the two-phase flow pattern at the impeller intake region. The size of bubbles in this region is similar to those observed at the impeller channel. Thus, one may speculate the bubble breakup is not a relevant factor at this operating condition.

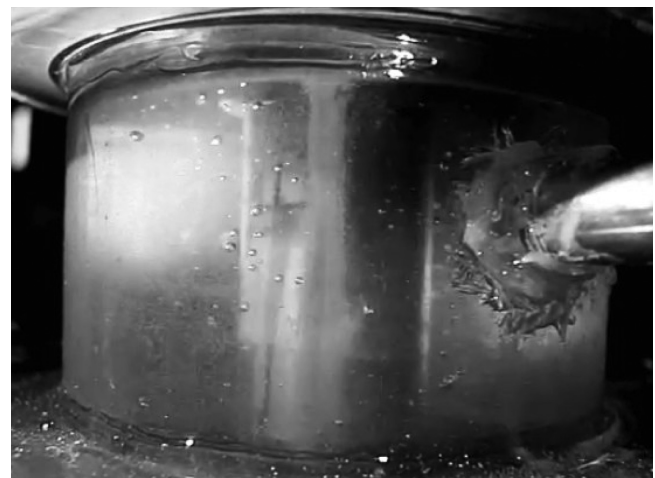


Figure 18. Isolated Bubbles (Regime I, Point (1), Figure 16) at Intake.

Bubbly Flow (Regime I, Point (2), Figure 16)

As the volumetric gas fraction is increased to point (2), the bubble size and numbers of bubbles have increased significantly, as is observed in Figure 19. Therefore, this flow pattern has been denoted as bubbly flow. The smallest bubbles are seen flowing close to the back shroud, so that they quickly move to the diffuser and leave the impeller. Another group of bubbles of intermediate size flows in the region between half of the channel height and the back shroud.

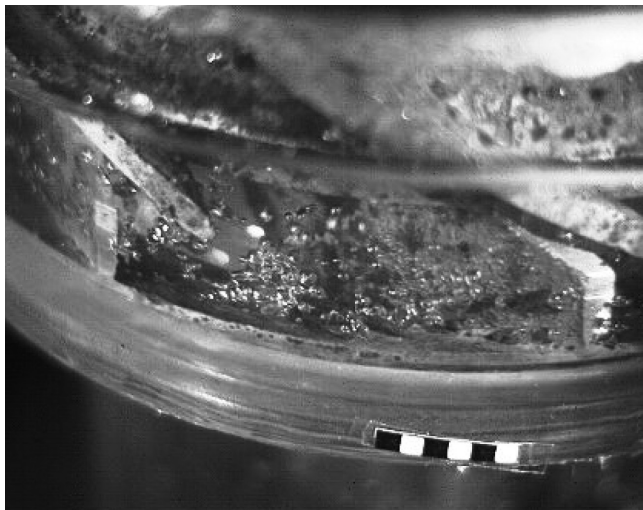


Figure 19. Bubble Flow (Regime I, Point (2), Figure 16).

These bubbles can be either dragged out toward the diffuser or trapped in the recirculation that is explained at the end of this section. The third group of bubbles has the largest size and it flows close to the front shroud. These bubbles follow a “preferential” path inside the impeller, which goes from the trailing face of the channel (or low pressure side) to leading channel face (or high pressure side). Indeed, it is observed that the bubbles follow a liquid stream line that goes across the channel.

Due to the increase of the bubble size and their population, the interaction between bubbles is more noticeable and even clusters or agglomerations of bubbles are observed in the channel. Similarly, the size of bubbles and their population has increased in the intake region as is presented in Figure 20. The bubbles at that region have an equivalent volume spherical diameter as large as 4 mm, and more interaction between bubbles is observed.



Figure 20. Bubble Flow (Regime I, Point (2), Figure 16) at Intake.

When the largest bubbles get into the impeller, they go to a certain region on the trailing face of the channel, where these bubbles are broken into finer ones. Therefore, the bubbles with smaller sizes are seen inside the impeller rather than in the intake region. The bubble breakup is more severe for this operating condition. Based on the results presented so far, one can argue that the bubble breakup in an ESP occurs only if the bubble size at the intake reaches a certain critical value.

Gas Pocket (Regimes II and III, Point (4), Figure 16)

Further increase of the volumetric gas fraction up to points (3) and (4) causes surging in the stage. Although the volumetric gas fraction is the same for both points, the corresponding impeller flow pattern is completely different. The impeller flow pattern in point (3) matches the description of the flow pattern in point (2) as shown in Figure 21.

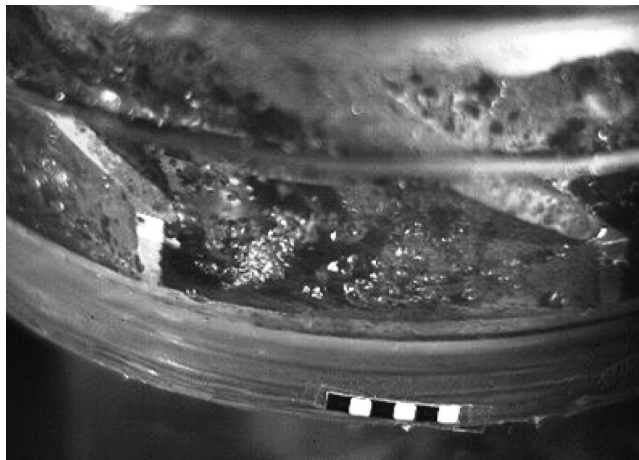


Figure 21. Bubble Flow (Regime I, Point (3), Figure 16).

There is more interaction between bubbles and a bubble cluster seems to be tighter than in the previous condition. The operation in point (3) only lasts for some minutes and then the head drops to point (4) without a change in the volumetric gas fraction. The stage operation at point (4) can last indefinitely indicating point (3) is an unstable operating condition.

The flow pattern inside the impeller at point (4) is presented in Figure 22. A gas pocket is now observed inside the impeller channel, which extends from the trailing face until the middle of the channel. This gas pocket is located close to the front shroud so the region above and to the right of the gas pocket is occupied by the water. This pocket can be seen in every impeller channel.

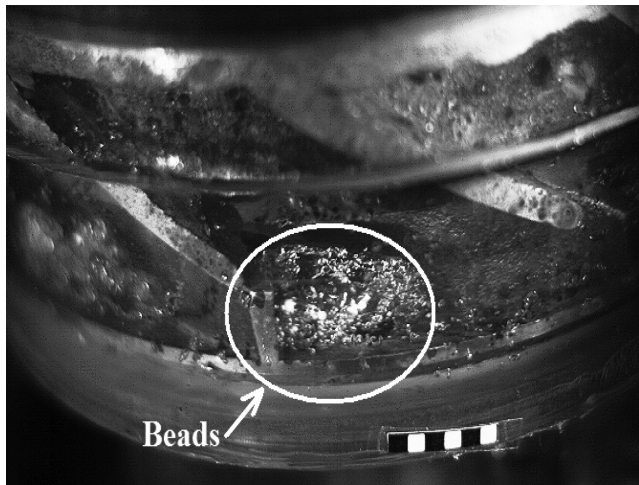


Figure 22. Gas Pocket (Regimes II and III, Point (4), Figure 16).

Dispersed bubbles are no longer seen in the area around the gas pocket. This implies that the gas bubbles are being mixed somewhere within the gas pocket. Thus, the gas flows through the gas pocket as a “continuous” phase. This statement is confirmed in the videos recorded when the gas is injected directly to the second stage and Styrofoam beads are injected through port #3. These beads do not move through the area around the gas pocket but they flow through the gas pocket itself as shown in Figure 23.

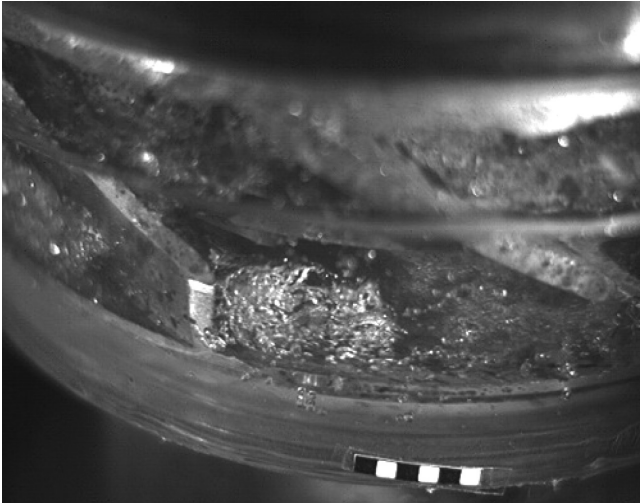


Figure 23. Foam Beads into Gas Pocket.

In the videos, it is observed that the beads are trapped into the gas pocket and move toward the impeller exit through it. They escape from the gas pocket at the region without a back shroud, where they break into fine bubbles. It means the bubbles coalesce creating a new continuous gas phase inside the impeller instead of a stationary gas pocket with no interaction with the surrounding bubbles. Two separated phases then flow through the impeller for volumetric gas fractions greater than the surging one.

The gas pocket is formed only in the region enclosed between both shrouds. In the region without a back shroud, the gas pocket is dispersed into fine bubbles, whose behavior follows the description of point (2). Thus, the bubbles that leave the impeller are produced due to a different mechanism than those before the surging.

Some authors, such as Thum, et al. (2006), have stated that the gas pocket formation is associated with a switch in the flow pattern at the intake region of the pump. Figure 24 shows that the gas is dispersed as bubbles in the intake region for the operation conditions of points (3) and (4). Therefore, the gas pocket formation is not caused by the transition of the gas and liquid flow pattern at the intake.



Figure 24. Gas Pocket (Regimes II and III, Point (4), Figure 16) at Intake.

Segregated Gas (Regime IV, Point (5), Figure16)

Even further increment of the volumetric gas fraction causes a reduction of the stage head until point (5). The gas pocket at this operating condition grows and occupies a larger volume-area inside the impeller, as is shown in Figure 25. Bursts of gas come out from

the side of the gas pocket that is closer to the trailing face. It breaks into fine bubbles that move quickly out of the impeller toward the diffuser.

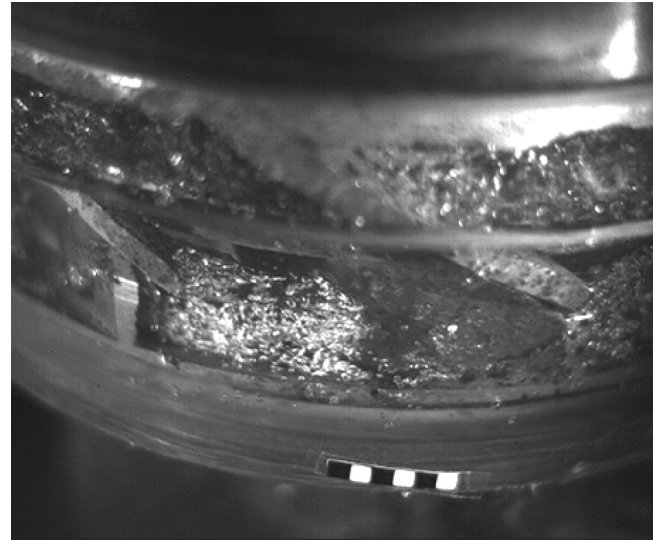


Figure 25. Segregated Gas (Regime IV, Point (5), Figure 16).

Another gas burst comes out from the gas pocket near the middle of the impeller channel. Again, this burst is broken into fine bubbles, but these bubbles do not flow out of the impeller immediately. Instead, these are dragged into the impeller recirculations by the liquid. The bubbles generated by gas bursts can be classified into two groups: spherical and ellipsoid. The ellipsoidal bubbles look prolate right after detaching from the gas pocket, but they seem to deform into oblate ellipsoids in the diffuser.

Significant movement is observed in the gas pocket surface, which constantly changes in shape and size. This interface does not seem to be attached to any of the impeller walls. Thus, there is a balance among the internal pressure, the surface tension, and shear that maintains the integrity of the gas pocket. Once again, Figure 26 proves that the gas is “dispersed” into bubbles in the intake region, even when the gas pocket is formed into the impeller channels.



Figure 26. Segregated Gas (Regime IV, Point (5), Figure 16) at Intake.

The impeller flow patterns description presented so far is valid at other liquid flow rates and other rotational speeds. However, the interpretation of the surging changes according to the liquid flow rate. Figure 27 shows photos taken at surging conditions for

normalized liquid flow rates between 0.8 and 0.6. The relative position of the impeller with respect to the diffuser is the same in every photo for comparison purposes.

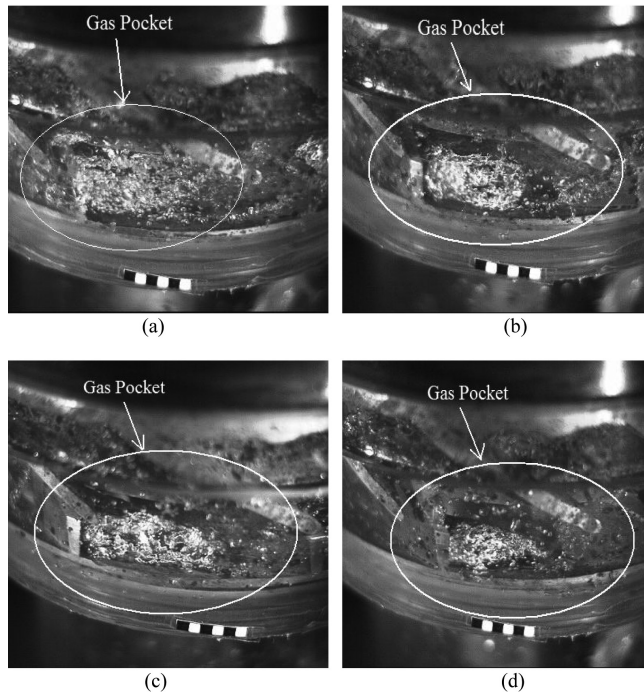


Figure 27. Gas Pocket Comparison at 600 rpm: (a) 0.2, (b) 0.4, (c) 0.6, (d) 0.8.

In these photos, one can notice that at high liquid flow rate (Figure 27d) the gas pocket occupies a small portion of the total volume of the channel. This pocket is flat and very close to the front shroud such that the liquid can flow through the upper region above the gas pocket. The small bubbles coming out from the pocket close to the front shroud and the leading face of the channel reveal that the liquid flows through these spaces, too.

The gas pocket for a normalized liquid flow rate of 0.6 has grown, occupying a larger volume-area within the impeller (refer to Figure 27c). Although, the gas pocket continues close to the front shroud, the region above the gas pocket is smaller. Thus, the effective area through which the liquid flows is reduced. Again, the bubbles from the gas pocket indicate that the liquid flows underneath the pocket and through the space between the leading face and the gas pocket.

Figure 27b shows the gas pocket for 0.4 normalized liquid flow rate. It has grown and now occupies most of the region between the gas pocket and the back shroud, so that the effective flowing area for the liquid is much smaller. As a result, the liquid flows through the clearance between the gas pocket and the leading face, producing a large burst of gas bubbles into that region.

For a normalized liquid rate of 0.2, the gas pocket blocks the region above it causing the effective flowing area for the liquid to reduce drastically. This gas pocket can extend out of the region enclosed between both shrouds up to the impeller exit, along the impeller vane. At this operating condition, there is a clear contact between the impeller walls and the gas pocket at the exit region, which implies that the interface now occurs among three phases: gas, liquid, and solid.

During the tests for 0.2 normalized liquid flow rate, it is observed that gas bubbles flow back into the intake region as illustrated in Figure 28. The bubbles get into the impeller and then are broken into finer ones. These new bubbles or “daughter bubbles” do not flow through the impeller but return to the intake, which is observed at any gas rate for this normalized liquid rate.



Figure 28. Bubbles at Intake Region at 0.2.

The bubbles eventually flow into the impeller, but then they are replaced by new ones so the bubble population remains in equilibrium. These bubbles do not collide with the other ones coming from the previous stage. It is hard to determine why the bubbles do not collide, but one can speculate that the bubbles flowing back orbit in a circular path that is far away from the core of bubbles coming in.

This phenomenon increases the residence time of the bubble within the impeller, which causes an increase in the actual gas fraction in the impeller. It may explain why the surging is triggered at lower volumetric gas fractions for this normalized liquid rate.

DISCUSSION OF RESULTS

Performance Map and Impeller Flow Patterns

The normalized performance map proposed by Romero (1999) and Gamboa (2009) is utilized to map the prototype performance at 600 rpm with air injection through first stage at 2 psig (visualization stage intake pressure). For this map, shown in Figure 29, the surging is determined from the operating conditions at which a performance breakdown occurs, for each normalized liquid flow rate. The second boundary is determined when the gas pocket becomes stable within the impeller, which is observed in the videos only for a normalized liquid flow rate of 0.8. Because the gas pocket is different for 0.2 normalized liquid flow rate, the third boundary is set at this normalized liquid flow rate. The visual observations are utilized to define the flow pattern in the impeller channel within each performance region.

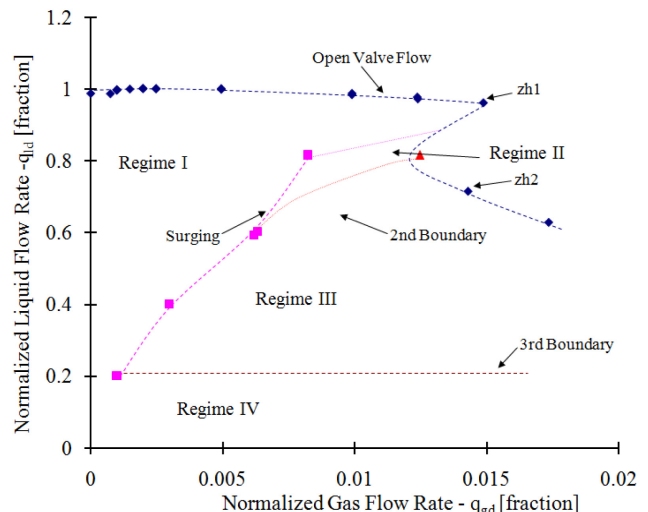


Figure 29. Visualization Performance Map at 2 psig, 600 rpm.

The open valve flow boundary in Figure 29 is obtained from a special test, keeping the zero pressure rise at the stage by varying the liquid flow rate every time the gas rate is increased. Points zh1 and zh2 in Figure 29 occur approximately at the same normalized gas flow rate. However, both differ in the normalized liquid flow rate for zero pressure rise. Figure 30b shows that the impeller flow pattern at zh1 is bubbly, which is in contrast to the gas pocket observed at zh2 as is shown in Figure 30a. This confirms that a flow pattern transition occurs at zero pressure rise. It demonstrates that the gas pocket formation, due to the surging, is strongly related to a bubble coalescence process that varies with the rotational speed, pressure rise and fluid properties.

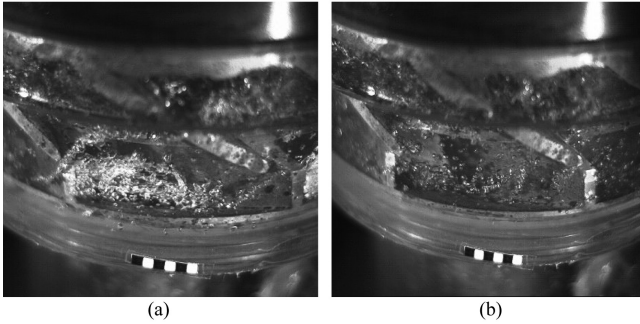


Figure 30. Impeller Flow Patterns: (a) at zh2, and (b) at zh1 (Figure 29).

It is observed that the gas pocket flow pattern is split in two sub-regimes, namely, unstable gas pocket and stage gas pocket based on the gas pocket behavior observed in the videos.

These results demonstrate that the performance map based on the performance curve is a consequence of the impeller flow patterns. The boundaries in this map are transitions between flow patterns inside the impeller. Thus, a theoretical mechanistic performance map can be developed based on the modeling of those transitions as is mentioned by Gamboa (2009).

Effect of IPA on the Gas Pocket Stabilization

A pressure recovery is observed in the performance curve with alcohol aqueous solution and air following the surging. This phenomenon does not occur in any of the other performance curves. In order to investigate the cause of this head recovery, a series of photos is presented from Figure 31 through Figure 34.

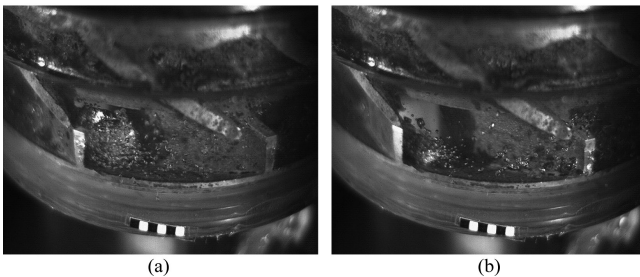


Figure 31. Impeller Flow Pattern at 0.24 Percent.

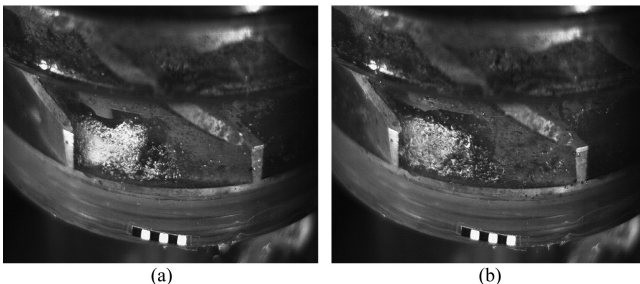


Figure 32. Impeller Flow Pattern at 0.32 Percent.

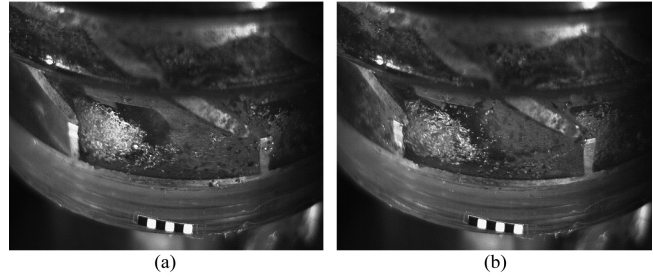


Figure 33. Impeller Flow Pattern at 0.4 Percent.

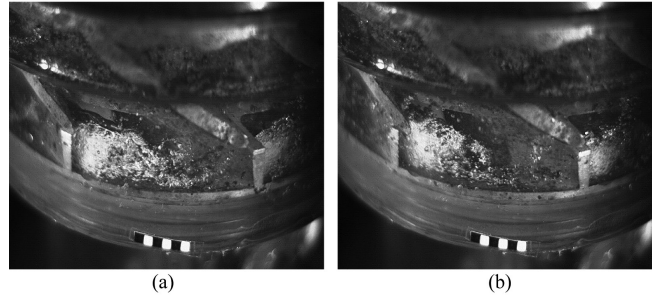


Figure 34. Impeller Flow Pattern at 0.81 Percent.

Figure 31a shows the impeller flow pattern at the surging for a volumetric gas fraction of 0.24 percent, while Figure 31b shows the same channel after one revolution. Notice that the gas pocket visible in Figure 31a is broken, after one revolution, as shown in Figure 31b. This implies that this gas pocket is unstable, whereby it is constantly formed and broken. In fact, two out of the seven channels do not have a gas pocket.

Figure 32a shows the impeller flow pattern at 0.32 percent volumetric gas fraction, which is the volumetric gas fraction before the head recovery occurs. It is noticeable that the gas pocket has grown and it has taken over more volume-area inside the impeller channel. As before, Figure 32b shows the same channel after one spin of the impeller. In both figures, one can observe a well-formed gas pocket, for which does not break up so it can be considered as “stable.” For this case, the gas pocket is observed in six out of seven channels.

Figure 33a presents the impeller flow pattern at a volumetric gas fraction of 0.4 percent at which condition the pressure recovery occurs. One expects the gas pocket is larger than in the previous operating condition because the volumetric gas fraction has increased. However, it is actually slightly smaller, so that the flowing area between the leading face of the channel and the gas pocket has grown. Figure 33b shows the same gas pocket after one impeller spin. The gas pocket is not dispersed, but rather is stable inside the channel. However, this gas pocket is not stable in other channels where it is dispersed into bubbles. Indeed, three out of seven channels have unstable gas pockets.

A gas pocket is observed in every channel of the impeller at 0.81 percent volumetric gas fraction as shown in Figure 34. As is expected, this gas pocket has grown and taken over a greater volume-area of the channel. The gas pockets are stable in every channel and look flatter and closer to the front shroud, as compared to the previous condition.

This sequence of photos shows that the pressure recovery may be associated with a variation of the gas pocket shape, stability and relative location in the impeller channel. The gas pocket varies its shape and relative position inside the channel at a volumetric gas fraction of 0.4 percent. Hence, it becomes unstable and is dispersed in most of the impeller channels, opposite to what one can expect. Thus, the only conclusion that can be derived from this analysis is that the stage performance is strongly affected by the interfacial stability of the gas pocket and the interfacial phenomena between the phases.

CONCLUSIONS

- The data acquired demonstrate clearly the effect of volumetric gas fraction (λ), rotational speed, gas density and surface tension on an ESP two-phase pump performance.
- The rotational speed and intake pressure affect the critical λ at the surging conditions. Increasing the rotational speed moves the critical λ (and surging) to higher values, expanding the pump operational window. Similarly, increasing intake pressure results in higher critical λ and expanded operational window of the pump. Also, increasing the rotational speed does not affect the pump performance before the surging.
- Flow visualization and video recording through the transparent prototype stage shed light on the two-phase flow behavior phenomena in an ESP. These include the effect of fluid properties (gas density and surface tension) on the flow behavior and stage performance. Also, the formation of a stagnant gas pocket that causes the surging is observed. For high liquid flow rates, the surging is associated with a gas pocket unstable, leading to an unstable stage performance, while the surging at low liquid flow rates is related to a stable gas pocket that can be segregated to the back shroud of the impeller.
- The gas pocket formation at zero head demonstrates that it is a consequence of a bubble coalescence phenomenon, which is an alternative to the bubble trap approach proposed by Sachdeva (1990). It may help to formulate new correlations and models for predicting the surging.
- The test demonstrates the bubble size at the stage inlet plays a key role on the two-phase performance of an ESP. It explains the difference in performance between a single stage and multistage arrangement.
- The addition of surfactant has a tremendous impact on the bubble size within the pump and on its performance. The IPA promotes a "noncoalescing" system, which is observed in the performance as a displacement of the surging at high volumetric gas fraction.
- The latter result may have a practical application in subsea boosting applications where a surfactant such as MEG corrosion inhibitor is commonly utilized. The surfactant injection may be applied at the pump intake, which may improve the two-phase performance and extend the pump operating window.

REFERENCES

- API RP 11S2, 1997, "Recommended Practice for Electric Submersible Pump Testing," Second Edition. American Petroleum Institute, Washington, D.C.
- Barrios, L., 2007, "Visualization and Modeling of Multiphase Performance Inside an Electrical Submersible Pump," Ph.D. Dissertation, Petroleum Engineering Department, The University of Tulsa.
- Downham, S. E., 2000, "Modeling the Two Phase Performance of a Centrifugal Pump," Ph.D. Dissertation, Cranfield University.
- Dunbar, C.E., 1989, "Determination of Proper Type of Gas Separator," Microcomputer Applications in Artificial Lift Workshop, SPE Los Angeles Basin Section.
- Duran, J., 2003, "Pressure Effects on ESP Stages Air-Water Performance," M.S. Thesis, The University of Tulsa.
- Estevam, V., 2002, "Uma Análise Fenomenológica da Operação de Bomba Centrífuga com Escoamento Bifásico," (A Phenomenological Analysis about Centrifugal Pump in Two-Phase Flow Operation), Ph.D. Dissertation, Universidade Estadual de Campinas.
- Gamboa, J., 2009, "Prediction of The Transition in Two-Phase Performance of an Electrical Submersible Pump," Ph.D. Dissertation, Petroleum Engineering Department, University of Tulsa.

- Hu, B. A, Nienow, E., Hugh, A, and Pacek, 2006, "Bubble Sizes in Agitated Solvent/Reactant Mixtures Used in Heterogeneous Catalytic Hydrogenation of 2-Butyne-1, 4-Diol," *Chemical Engineering Science*, 61, pp. 6765-6774.
- Lea, J. F. and Bearden, J. L., 1980, "Effect of Gaseous Fluids on Submersible Pumps," Paper presented at SPE 55th Annual Fall Technical Conference and Exhibition, SPE 9218, pp. 2922-2930.
- Manzano-Ruiz, J., 1980, "Experimental and Theoretical Study of Two-Phase Flow," Ph.D. Dissertation, Massachusetts Institute of Technology.
- Murakami, M. and Minemura, K., 1974a, "Effects of Entrained Air on the Performance of Centrifugal Pumps (2nd Report, Effects of Number of Blades)," *Bulleting of the JSME*, 17, (112), pp. 1286-1295.
- Murakami, M. and Minemura, K., 1974b, "Effects of Entrained Air on the Performance of Centrifugal Pumps (1st Report, Performance and Flow Conditions)," *Bulleting of the JSME*, 17, (110), pp. 1047-1055.
- Murakami, M. and Minemura, K., 1983, "Behavior of Air Bubbles in an Axial-Flow Pump Impeller," *Journal of Fluids Engineering*, 105, pp. 277-283.
- Pessoa, R., 2001, "Experimental Investigation of Two-Phase Flow Performance of Electrical Submersible Pump Stages," M.S. Thesis, The University of Tulsa.
- Ray, S., 1997, *High Speed Photography and Photonics*, Focal Press.
- Redlich, O. J. and Kwong, N. S., 1949, "On the Thermodynamics of Solutions. V. on Equation of State. Fugacities of Gaseous Solutions," *Chemical Reviews*, 44, pp. 233-244.
- Romero, M., 1999, "An Evaluation of an Electric Submersible Pumping System for High GOR Wells," M.S. Thesis, The University of Tulsa.
- Sachdeva, R., 1990, "Two-Phase Flow through Electric Submersible Pumps," M.S. Thesis, The University of Tulsa.
- Sato, S., Furukawa, A., and Takamatsu, Y., 1996, "Air-Water Two-Phase Flow Performance of Centrifugal Pump Impellers with Various Blade Angles," *JSME International Journal*, 39, (2), pp. 223-229.
- Thum, D., Hellmann, D. H., and Sauer, M., 2006, "Influence of the Patterns of Liquid-Gas Flows on Multiphase-Pumping of Radial Centrifugal Pumps," Fifth North American Conference on Multiphase Technology, pp. 79-90.
- Zapata, L., 2003, "Rotational Speed Effects on ESP Two-Phase Performance," M.S. Thesis, The University of Tulsa.

BIBLIOGRAPHY

- Gülich, J. F., 2008, *Centrifugal Pumps*, Berlin: Springer-Verlag.
- Kensington, N., 1941, *The Physics and Chemistry of Surface*, Third Edition, Oxford University Press.
- Kenyery, F., 2008, "ESP CFD Simulation for High Flow Rate," Mechanical Engineering Department, Universidad Simon Bolivar, Caracas, Venezuela, Unpublished.
- Meissner, H. P. and Michaels, A. S., 1949, "Surface Tensions of Pure Liquids and Liquid Mixtures," *Industrial Engineering Chemistry*, 41, pp. 2782-2787.
- Minemura, K., and Uchiyama T., 1993, "Three-Dimensional Calculation of Air-Water Two-Phase Flow in Centrifugal Pump Impeller Based on a Bubbly Flow Model," *Journal of Fluids Engineering*, 115, pp. 766-771.

- Rasmussen, K., 1997, "Calculation Methods for the Physical Properties of Air Used in the Calibration of Microphones," Report PL-11b Published by Department of Acoustic Technology, Technical University of Denmark.
- Sengers, J. and Dooley, B., 1992, "Equations for the Thermodynamic Properties of Ordinary Water Substance at Saturation," The International Association for the Properties of Water and Steam, St. Peterburg, Russia.
- Stepanoff, A. J, 1957, *Centrifugal and Axial Flow Pump: Theory, Design, and Application*, Second Edition, New York, New York: John Wiley & Sons.

ACKNOWLEDGEMENT

The authors are grateful to Tulsa Artificial Lift Project and its member companies for financial support. The authors would like to thank the technical support and suggestions of Dr. Ovadia Shoham and Mr. Bruno Schiavello.